

# Experimental study of forces between quasi-two-dimensional emulsion droplets near jamming

Kenneth W. Desmond<sup>a</sup>, Pearl J. Young, Dandan Chen<sup>b</sup>, Eric R. Weeks\*

We experimentally study the jamming of quasi-two-dimensional emulsions. Our experiments consist of oil-in-water emulsion droplets confined between two parallel plates. From the droplet outlines, we can determine the forces between every droplet pair to within 8% over a wide range of area fractions  $\phi$ . We study three bidisperse samples that jam at area fractions  $\phi_c \approx 0.86$ . Our data show that for  $\phi > \phi_c$ , the contact numbers and pressure have power-law dependence on  $\phi - \phi_c$  in agreement with the critical scaling found in numerical simulations. Furthermore, we see a link between the interparticle force law and the exponent for the pressure scaling, supporting prior computational observations. We also observe linear-like force chains (chains of large interdroplet forces) that extend over 10 particle lengths, and examine the origin of their linearity. We find that the relative orientation of large force segments are random and that the tendency for force chains to be linear is not due to correlations in the direction of neighboring large forces, but instead occurs because the directions are biased towards being linear to balance the forces on each droplet.

## 1 Introduction

A liquid to amorphous-solid transition, also known as a jamming transition, occurs in a wide variety of soft materials such as colloids, emulsions, foams, and sand. In general the jamming transition is due to an increase in the particle concentration  $\phi$ ; the particles become sufficiently crowded so that microscopic rearrangements are unable to occur when external stresses are applied<sup>1–3</sup>. At a critical  $\phi_c$  the system jams into a rigid structure, and many of the material properties are known<sup>2,4</sup> to scale with a power-law dependence on  $(\phi - \phi_c)$ . While these soft materials have obvious differences, it has been postulated that there are universal features of the jamming transition that all these materials share in common such as critical scaling and the emergence of force chains.

In all systems above the jamming point, particles press into one another and deform. As the density increases, new contacts form and particles deform more, increasing the pressure. Interesting, both the average number of contacts  $z$  and the pressure  $P$  show critical-like scaling relative to the jamming point. In experiments and simulations, both 2D and 3D, the average number of contacts scales as  $z - z_c = A(\phi - \phi_c)^{\beta_z}$ , where  $z_c$  and  $A$  depend on the dimension and  $\beta_z = 1/2$  regardless of dimension<sup>5–11</sup>. Simulations found  $P \sim (\phi - \phi_c)^{\beta_P}$ , where  $\beta_P$  depends on the details on the interparticle force law<sup>5–8</sup>. If this pressure scaling and connection between  $\beta_P$  and the interparticle force law extends to experiments, then this would demonstrate a direct link between the interaction of the constituent particles and the bulk properties of the sample, as the bulk modulus can be found from  $P(\phi)$ .

Another observed feature of jammed systems is the spatial heterogeneity of the particle-particle contact forces. In experiments and simulations, both 2D and 3D, the shape of the probability distribution of forces is broad with an exponential like tail<sup>7,8,10–21</sup>. The largest forces tend to form chain structures that bear the majority of the load<sup>12–18</sup>. These force chains are responsible for providing rigidity of jammed materials to external stresses and are related to many other bulk properties<sup>12,13,22,23</sup>. In prior experiments on 3D emulsions, the structure of the force chains was studied directly, where force chains extended over 10 particle diameters with an persistence length of 3 - 4 particle diameters<sup>15,19,20</sup>.

There have been theoretical attempts to understand force chains, such as the q-model of Coppersmith *et al.*<sup>24</sup>, directed-force chain networks of Socolar's group<sup>25</sup>, and simulations<sup>26–28</sup>. Others took an ensemble approach to describe force chains, with different choices for ensembles<sup>20,29–35</sup>. While some of these models successfully predict certain properties of the force network, they can not explain the physical origins of force chains. To explain the structure of the force chains observed in 3D emulsion studies, Brujić *et al.*<sup>19,20</sup> and Zhou *et al.*<sup>15,32</sup> proposed an accurate model that provides a physical description for the origin of force chains. This model has two simple assumptions: first, the forces on a droplet must balance, and second, forces between neighboring droplets are uncorrelated. This model has not been applied to 2D systems.

In this paper, we introduce a new experimental system to study the universal nature of the jamming transition. Our system consist of quasi-2D soft deformable droplets with no static friction forces. In the appendix, we describe our method to determine the forces between droplets in contact to within 8%, significantly better than prior studies of foams<sup>11</sup> and comparable to photoelastic disks<sup>14</sup>. Using our experimental model system, we find power-law scaling for the coordination num-

Department of Physics, Emory University, Atlanta, GA 30322, USA.

<sup>a</sup> Current address: Department of Mechanical Engineering, University of California, Santa Barbara, CA 93106, USA.

<sup>b</sup> Current address: Soochow University, Suzhou, Jiangsu, China

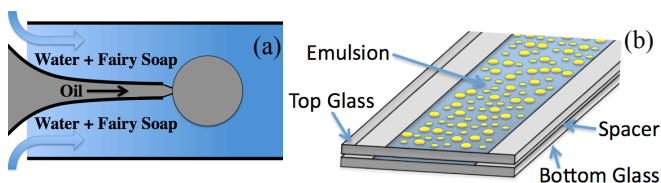


**Fig. 1** (Color online) (a) A schematic of our co-flow apparatus. Oil is pumped at a constant rate through a micropipet centered within a capillary tube of larger diameter. Around the inner micropipet, a 5 g/mL water Fairy soap mixture is pumped through the capillary tube, and as oil leaves the micropipet it forms spherical droplets that repeatedly break off with the same diameter. (b) A schematic of our sample chamber where emulsion droplets are confined to a 2D plane by two microscope slides separated by either a  $\sim 100 \mu\text{m}$  spacer (transparency film) or  $\sim 180 \mu\text{m}$  spacer (glass coverslip).

ber and pressure (Sec. 4.2), we observe a relationship between the interparticle force law and  $\beta_P$  (Sec. 4.2), and see a distribution of contact forces similar to prior work (Sec. 4.3). Further, we confirm the assumptions of the Bruijic-Zhou model apply to our data and that the model well-describes our 2D data (Sec. 4.4). This work provides an in depth study comparing data from our experimental model system to other numerical simulations, theory, and experimental systems, thus furthering our understanding of the jamming transition and supporting the applicability of ideas of jamming to a new system.

## 2 Experimental method

We produce emulsions using a standard co-flow micro-fluidic technique<sup>36</sup>, see Fig. 1(a). The inner tube diameter is  $\sim 35 \mu\text{m}$  and the outer tube diameter is  $\sim 500 \mu\text{m}$ . The continuous phase is a mixture of water and the commercial soap ‘‘Fairy’’, and flows through the outer tube at a rate of  $\sim 1 \text{ mL/min}$ . The droplets are mineral oil, which flows through the inner tube at a rate of  $\sim 0.5 \mu\text{L/hr}$ . Slight variations of these parameters let us produce monodisperse droplets with radii in the range of  $80\text{--}170 \mu\text{m}$ ; any given batch of droplets has a polydispersity of less than 4%. Mixing together two monodisperse batches lets us produce bidisperse samples with whatever size ratio and number ratio desired.

Our sample chamber is designed to create a system of quasi-2D emulsion droplets, analogous to 2D granular systems of photoelastic disks<sup>14</sup> but without static friction. The chamber consists of two microscope glass slides of dimensions  $25 \text{ mm} \times 75 \text{ mm}$  (Corning) separated by a  $\sim 100 \mu\text{m}$  spacer (transparency film) or a  $\sim 180 \mu\text{m}$  spacer (Corning No. 1 glass coverslip) glued along the two longer edges; see Fig. 1(b). The sample chamber thickness is tuned so that the droplets are deformed into pancake shapes, with aspect ratio (diameter/height) ranging from 1.6 to 3.0; see Fig. 12.

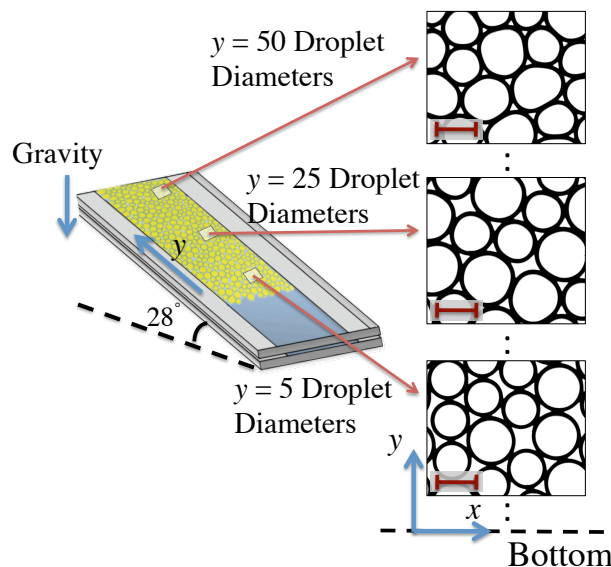


**Fig. 2** (Color online). Illustration of our experiment. Oil droplets rise to the top of the sample chamber due to buoyancy. At the bottom of the droplet ‘‘pile,’’ droplets barely touch and are not deformed. At the top, droplets are compressed due to the buoyant weight of the droplets below them. This lets us study the sample from the jamming area fraction on up, and also provides a means to calibrate the forces as described in the Appendix. The scale bar is  $200 \mu\text{m}$ , and the images have area fractions  $\phi = 0.88, 0.92, \text{ and } 0.96$ .

After the sample chambers are filled, they are placed on a microscope for imaging with either a  $1.6\times$  or  $5\times$  objective lens. The droplets are allowed to equilibrate their positions; we only consider static samples. Our camera takes  $2,200 \times 1,800 \text{ pixel}^2$  images. We overlap images from different areas to construct a single large field of view image on the order of  $10,000 \times 50,000 \text{ pixel}^2$  containing between 1,000 to 5,000 droplets depending on the droplet sizes. We image every droplet (wall-to-wall) and only analyze droplets more than  $\sim 4$  diameters away from the nearest wall to avoid wall effects<sup>37</sup>.

## 3 Empirical Force Law

We wish to use the droplet images (such as those shown in Fig. 2) to determine the forces droplets exert on each other. An isolated droplet is circular with 2D radius  $r_0$  due to surface tension. Droplets feeling forces from other droplets are deformed. Our goal is not to know the exact form of the force law governing inter-droplet forces. Rather, we need to know these forces to within our experimental error. The details of our approach are given in the Appendix; we briefly summarize our method here.

By tilting the sample as shown in Fig. 2, we exploit the known buoyant forces on the droplets, which are  $O(10^{-3} \mu\text{N})$

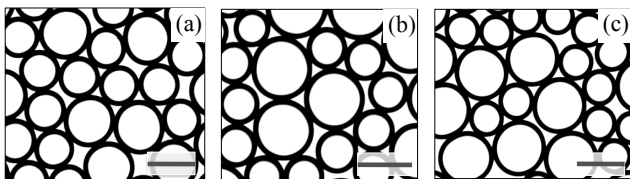


**Fig. 3** Close up view of regions within our three bidisperse samples. The scale bar in each image is  $250 \mu\text{m}$ . (a) is an image for our sample with size ratio 1.25 at  $\phi = 0.89$ . (b) is an image for our sample with size ratio 1.42 at  $\phi = 0.90$ . (c) is an image for our sample with size ratio 1.52 at  $\phi = 0.90$ .

per droplet. Droplets further up the incline feel larger forces and deform more because they must support the buoyant weight of the droplets below. This can be seen in Fig. 2, where droplets further up the incline are more compressed.

The key parameters to determine the forces are the contact length  $\Delta l$  of the interface shared between the two droplets, and the modified radius of curvature  $r$  of each droplet deduced from the perimeters of the droplets where they are not contacting another droplet. Laplace’s Law relates the interface curvature to the pressure difference between the interior and exterior of a droplet; in 3D this relation is  $\Delta P = \gamma/r$  with  $\gamma$  being the surface tension. From this, it is clear that deforming a droplet (increasing its internal pressure) results in  $r < r_0$ . Likewise, it is clear from Fig. 2 that  $\Delta l$  is larger for droplets feeling larger forces (droplets farther up the incline).

To find a force law from our data, we use numeric methods to find a force law  $f(\Delta l, r)$  that best satisfies what we know about the data: (1) the net force on any droplet is zero (as the droplets are motionless), (2) the components of the forces in the  $y$  direction balance the buoyant weight of each droplet, and (3) the forces acting between two touching droplets are equal and opposite. After some work, we find for two droplets  $i$  and  $j$  in contact that the best functional form is

$$F = \alpha_1(R_0L/r_{ij}) + \alpha_2(R_0L/r_{ij})^2, \quad (1)$$

where  $1/r_{ij} = 1/r_i + 1/r_j$ ,  $R_0$  is the mean 3D droplet radius prior to putting the sample into the quasi-2D chamber, and  $\alpha_1$  and  $\alpha_2$  are constants that depend on the oil-water-surfactant details. For our samples,  $\alpha_1 = 4.25 \mu\text{N}/\text{mm}$  and  $\alpha_2 = 4.12 \mu\text{N}/\text{mm}^2$ . The forces we observe in the experiment range from  $0 - 0.5 \mu\text{N}$ , several hundred times larger than the buoyant weight of an individual droplet, which makes sense given that the inter-droplet forces at high  $\phi$  are due to the accumulated pressure from the buoyant forces of the many droplets below. Intriguingly, we find that the force law does not depend on the gap thickness of the sample chamber. We stress that Eqn. 1 is an empirical deduction and is only approximate. The data presented in the next section are from images taken with the  $1.6\times$  objective lens and the forces obtained have a random un-

$\sigma$	$n_r$	$r_0^{(\text{big})}$	poly <sup>(big)</sup>	$r_0^{(\text{small})}$	poly <sup>(small)</sup>
1.25	0.684	$126 \mu\text{m}$	3.4%	$102 \mu\text{m}$	3.1%
1.42	0.849	$130 \mu\text{m}$	3.0%	$105 \mu\text{m}$	3.4%
1.52	0.806	$137 \mu\text{m}$	3.3%	$90.1 \mu\text{m}$	3.1%

**Table 1** This table provides parameters characterizing the droplets in our 3 bidisperse samples. The first column  $\sigma = r_0^{(\text{big})}/r_0^{(\text{small})}$  is the size ratio and the second column is the number ratio  $n_r = N^{(\text{big})}/N^{(\text{small})}$ . The polydispersity in droplet sizes for the big droplets is indicated by poly<sup>(big)</sup> and for the small droplets by poly<sup>(small)</sup>. The polydispersity is defined as the standard deviation in droplet sizes normalized by the mean size. Our uncertainties are  $\pm 2 \mu\text{m}$  in  $r_0$ ,  $\pm 0.1\%$  in  $\sigma$ , and  $< 0.1\%$  in polydispersity. Since we image every single droplet there is no measurement error in  $n_r$ .

certainty of 16%. For a more detailed discussion on obtaining this force law and the uncertainty, see the Appendix.

## 4 Jamming of Binary Packings

We will investigate the jamming transition and force networks in disordered bidisperse packings using the setup shown in Fig. 2. By allowing the sample to equilibrate in this chamber, we set up a gentle gradient in area fraction ranging from just barely jammed at the bottom of the incline to well-jammed near the top. This lets us study the properties of the packing over this full range of area fractions. For the analysis in this section, we only consider droplets between 5 and 50 droplet diameters up the incline, unless otherwise specified. This region corresponds to an area fraction  $\phi$  ranging from 0.89 – 0.96. We study three different samples with different size ratios, as shown in Fig. 3. Details of each sample are given in Table 1.

### 4.1 Identifying jamming area fraction $\phi_c$

We start by identifying the jamming area fraction  $\phi_c$  for each data set. To determine the jamming point, we calculate the area fraction with distance up the incline directly from our images of the droplets in three steps. First, using the centers and radii of the droplets we compute the radical Voronoi cells<sup>38,39</sup> for each droplet. The radical Voronoi tessellation divides space into polygons, one per droplet, taking into account each droplet’s size so that each droplet is fully contained within its own polygon. Second, we determine the area  $A_v$  of each Voronoi cell and the area  $A_d$  of each droplet. Third, the area fraction  $\phi(y)$  at a position  $y$  is computed as  $\phi(y) = \sum_k A_{d,k} / \sum_k A_{v,k}$ , where  $k$  indexes all droplets with a center of mass within  $y - \Delta y/2$  and  $y + \Delta y/2$ . For this step, all the droplets are examined, down to nearly  $y = 0$ , except for the droplets at  $y \approx 0$  where the Voronoi cell is poorly defined.

We choose  $\Delta y = 6\langle r_0 \rangle$  where  $\langle r_0 \rangle$  is the mean droplet radius (which depends on the size ratio and number ratio, see Table 1 for details). This value of  $\Delta y$  gives roughly 150 droplets per  $y$  sampled. Within this window of  $\Delta y$ ,  $\Delta\phi = (\partial\phi/\partial y)\Delta y \approx 0.007$ . From  $\phi(y)$  we can obtain the jamming point  $\phi_c$  by extrapolating the value of  $\phi$  to  $y = 0$ , where  $y = 0$  is defined as the bottom of the droplet pile. We can treat the  $y = 0$  point in our data as the jamming point since the forces between droplets at  $y = 0$  are nearly zero. For the three data sets, the extrapolation is done by fitting  $\phi(y)$  to a power law [ $\phi(y) = \phi_c + ay^b$ ] giving  $\phi_c = 0.855 \pm 0.005$ ,  $0.861 \pm 0.005$ , and  $0.858 \pm 0.008$  for the data with size ratio  $\sigma = 1.25$ , 1.42, and 1.52, respectively. We chose to use  $\phi(y) = \phi_c + ay^b$  since  $\phi - \phi_c$  vs  $y$  appears fairly linear on a log-log plot. In simulations on frictionless disks and experiments on 2D foams it has been reported that  $\phi_c \sim 0.84$  for bidisperse systems<sup>7,11,37</sup>, which is a little lower than the values we found.

Our measured area fraction depends on where we define the outer perimeter of a droplet. As seen in Fig. 3, the droplets have thick black outlines. We look at the outer edge of each outline, and define the perimeter as the pixel location where the intensity is halfway between the white color outside the droplet, and the black color in the darkest part of the outline. The transition from black to white occurs over a distance of 2-3 pixels, and so we judge that we have a systematic uncertainty in the area fraction of roughly 1% due to the determination of the perimeter position. Since this is systematic, the distance to the jamming point ( $\phi - \phi_c$ ) is insensitive to this error and therefore in most of our results we focus on  $\phi - \phi_c$ .

## 4.2 Critical Scaling

The first critical scaling we investigate is the coordination number, the mean number of contacts each droplet has. Prior numerical studies of jamming in frictionless systems found that the coordination number  $z$  obeys a power law scaling of the form  $z - z_c = A(\phi - \phi_c)^{\beta_z}$ , where  $A \sim 3.5$ ,  $z_c = 4$ , and  $\beta_z = 1/2$ <sup>5-7</sup>. It has been observed that  $A$  has a slight dependence on the force law and polydispersity, but  $z_c = 4$  and  $\beta = 1/2$  are independent of the force law and polydispersity. Katgert *et al.*<sup>11</sup> found for a 2D bidisperse foam with size ratio 1.5 a critical scaling with  $A = 4.02 \pm 0.02$  and  $\beta_z = 0.50 \pm 0.02$  while fixing  $z_c = 4$ . The critical point  $z_c$  has been interpreted as the isostatic point  $z_{iso}$  (minimum number of contacts necessary for a mechanically stable packing). For 2D,  $z_{iso} = 4$ , in agreement with  $z_c$  found in prior work.

To compare experimental data and simulation data, the experimental area fraction needs to be converted into a theoretical area fraction<sup>11</sup>. This is because the simulated particles are allowed to overlap (thus diminishing the total area they take up at large  $\phi$ ) while our experimental droplets always occupy the same total area. We convert our experimental  $\phi$  values to

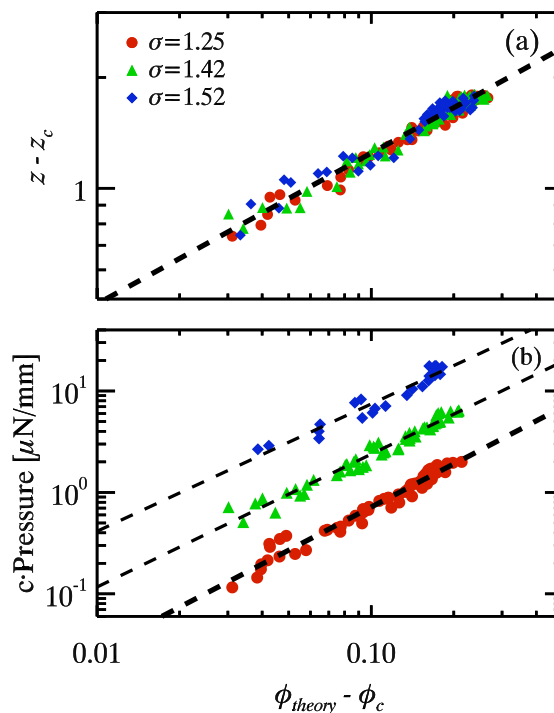


**Fig. 4** (Color online) (a) Scatter plot of coordination number against  $\phi_{theory} - \phi_c$ . All data were fitted together to  $z - z_c = A(\phi - \phi_c)^{\beta_z}$ , where the fit is shown as the black dashed line with fit parameters  $z_c = 4.2$ ,  $A = 3.2$ , and  $\beta_z = 0.4$ . Fitting the different data sets separately gives slightly different fit values, listed in Table 2. (b) A scatter plot between pressure and  $\phi_{theory} - \phi_c$ . The pressure has been scaled by  $c = 1, \sqrt{10}$ , and 10 for the  $\sigma = 1.25, 1.42$ , and 1.52 data respectively. Each data set is fitted to  $\mathcal{P} = A(\phi_{theory} - \phi_c)^{\beta_p}$ , shown as the black dashed lines. The fit values are given in Table 2.

$\phi_{theory}$  using the method of Katgert *et al.*<sup>11</sup>. From our data we determine  $z$  and  $\phi_{theory}$  at various points along the incline. The results are plotted relative to the jamming point in Fig. 4(a), and show power-law scaling. Fitting the each data set to the theoretical scaling law,  $z - z_c = A(\phi - \phi_c)^{\beta_z}$ , we obtain values for  $A$ ,  $z_c$ , and  $\beta_z$  which are reported in Table 2. Our values of  $A \approx 3.2$  are close to  $A \approx 3.5$  found in a numerical study by O'Hern *et al.*<sup>7</sup> for particles with size ratio 1.4. The fitted values for  $z_c$  are within the uncertainty of the previously found value of 4<sup>5-7,11</sup>. However, our droplets have a slight attraction which may result in a slightly tighter packing of droplets at  $\phi_c$  with a coordination number  $z_c > 4$ . Given our uncertainties of  $z_c$ , our data are consistent with both  $z_c = 4$  and  $z_c > 4$ . Finally, for each packing, the exponent  $\beta_z \approx 0.4$  agrees with the prior findings ( $\beta = 0.5$ ) to within our uncertainty, although we have a fairly large uncertainty in our exponents. Interestingly, in 2D photoelastic disk experiments, they found  $z - z_c = (\phi - \phi_c)^{\beta_z}$  with  $\beta_z = 0.53 \pm 0.03$  without needing to convert their exper-

$z - z_c = A_z(\phi_{\text{theory}} - \phi_c)^{\beta_z}$			
$\sigma$	$A_z$	$\beta_z$	$z_c$
1.25	$3.2 \pm 0.6$	$0.4 \pm 0.2$	$4.3 \pm 0.3$
1.42	$3.3 \pm 0.6$	$0.4 \pm 0.2$	$4.3 \pm 0.3$
1.52	$3.2 \pm 0.7$	$0.3 \pm 0.2$	$4.0 \pm 0.4$
$\mathcal{P} = A_P(\phi_{\text{theory}} - \phi_c)^{\beta_P}$			
$\sigma$	$A_P$ [ $\mu\text{N}/\text{mm}$ ]	$\beta_P$	
1.25	$19 \pm 1$	$1.41 \pm 0.03$	
1.42	$15 \pm 1$	$1.30 \pm 0.03$	
1.52	$13 \pm 2$	$1.26 \pm 0.07$	
$f_{ij} = F_0(\delta r_{ij}/d_{ij})^{\beta_f}$			
$\sigma$	$F_0$ [ $\mu\text{N}$ ]	$\beta_f$	
1.25	$2.3 \pm 0.2$	$1.27 \pm 0.03$	
1.42	$2.4 \pm 0.1$	$1.19 \pm 0.02$	
1.52	$2.0 \pm 0.1$	$1.15 \pm 0.03$	

**Table 2** The fitting parameters for the power law fits to the data for each size ratio  $\sigma$ . Note that simulations found  $\beta_P = \beta_f$ <sup>8</sup>; see text for a discussion. The uncertainties in the fit values are obtained by computing the standard error in each fitting parameter.

imental  $\phi$  to  $\phi_{\text{theory}}$ <sup>10</sup>, but  $A \sim 25$  for that study which is considerably different from our results. In their work, they were limited to area fractions close to  $\phi_c$  due to the difficulty of compressing their particles to high area fractions, while our data (and those of Ref.<sup>11</sup>) extend over a larger range of  $\phi$ .

The second critical scaling we investigate is the dependence of pressure  $\mathcal{P}$  with distance to the jamming point. Simulations of 2D particles found  $\mathcal{P} = A(\phi_{\text{theory}} - \phi_c)^{\beta_P}$ , where  $A$  and  $\beta_P$  depend on the form of the force law. In the numerical study by O’Hern *et al.*<sup>8</sup>, they used frictionless disks that interacted via the force law  $f_{ij} = F_0(\delta r_{ij}/d_{ij})^{\beta_f}$ , where  $F_0$  is a scale,  $\delta r_{ij}$  is the distance between two particles in contact, and  $d_{ij}$  is the sum of the radii of the particles in contact. They found that  $\beta_P = \beta_f$ . It is certainly possible that for other force laws, the scaling of pressure with  $(\phi - \phi_c)$  could be different. In particular, in our experiment, the force between two droplets is not a unique function of  $\delta r_{ij}$  but rather depends on the droplet perimeters which are influenced by all of their neighbors. In 2D photoelastic disk experiments  $\beta_P$  was found to be 1.1<sup>10</sup>. No prior experimental 2D studies have examined the scaling of  $\mathcal{P}$  for systems without static friction.

For our experiment, we compute the local pressure of our sample by first locating a set of droplets  $k$  within a window  $y - \Delta y/2$  and  $y + \Delta y/2$ . For these  $k$  droplets the pressure is  $\mathcal{P} = \sum_i \sum_{j>i} F_{ij} r_{ij} / \sum_k A_{k,v}$ , where  $i$  and  $j$  index all contacts on the  $k$  droplets and  $\sum_k A_{k,v}$  is the sum of the Voronoi areas of all  $k$  droplets<sup>8,40</sup>. In this formula,  $F_{ij}$  and  $r_{ij}$  are both taken to be positive scalars. Here we use  $\Delta y = 5r_0$ . In Fig. 4(b) we plot the pressure for all three packings against  $\phi_{\text{theory}} - \phi_c$ . These

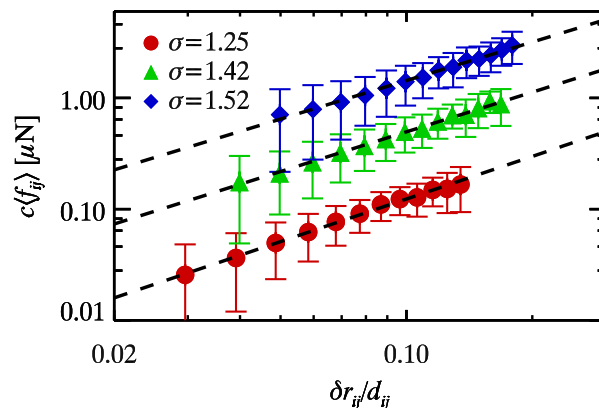


**Fig. 5** (Color online) The average force between droplets in contact plotted against the amount of compression between the droplets. The average force has been scaled by a prefactor of  $c = 1, \sqrt{10}$ , and 10 for the  $\sigma = 1.25, 1.42$ , and 1.52 data respectively. Each data is fitted to  $\langle f_{ij} \rangle = F_0(\delta r_{ij}/d_{ij})^{\beta_f}$  and the fits are shown as the black dashed lines. The fit values are given in Table 2. Note that this data is an effective force law, not the true force law: for a given  $\delta r_{ij}/d_{ij}$ , different droplet pairs may experience different contact forces. To illustrate this, we have added error bars to the plot, where the error bars represent one standard deviation in the spread of measured contact forces at each  $\delta r_{ij}/d_{ij}$ .

results show power-law scaling. The dashed lines are the fit to  $\mathcal{P} = A(\phi_{\text{theory}} - \phi_c)^{\beta_P}$  with the fit values shown in Table 2. In particular, we find  $\beta_P$  values between 1.26 - 1.41, larger than  $\beta_P = 1.1$  found for photoelastic disks<sup>10</sup>.

To compare with the simulations of O’Hern *et al.*<sup>8</sup>, we wish to approximate how forces between our droplets depend on their separations  $\delta r_{ij}$ . For each observed  $\delta_{ij}$  we find the true force  $f_{ij}$  from our force law. We average all of the observations over small windows in  $\delta_{ij}$  to find an effective average force law as a function of  $\delta_{ij}$ , plotted in Fig. 5. The error bars emphasize that Fig. 5 is only an average trend rather than the true force law. Intriguingly, the averaged data follow a power law: we fit each data to  $\langle f_{ij} \rangle = F_0(\delta r_{ij}/d_{ij})^{\beta_f}$  to obtain the power law exponent  $\beta_f$ . The fits are shown as the black dashed lines in the figure, with fit values listed in Table 2.

Our fits give  $\beta_f < \beta_P$  in contrast to the results of O’Hern *et al.*<sup>8</sup> where  $\beta_P = \beta_f$ . This equality was found for systems close to the jamming area fraction. The exponent for the pressure,  $\beta_P$ , relates to how droplets are compacted with increasing  $\phi - \phi_c$ <sup>9</sup>. Close to  $\phi_c$ , when  $\phi$  is slightly increased, droplets can avoid significant compression by rearranging and forming more contacts, however, at larger  $\phi$ , droplets can not form many new contacts and must instead undergo larger compression. Therefore, at larger area fractions, the pressure increases more rapidly with  $\phi - \phi_c$  than it does near the jamming point. This argument predicts  $\beta_P > \beta_f$ , in agreement with our data which extends far from  $\phi_c$ . While the uncertainty in each force



measurement is 16%, this uncertainty is unlikely to significantly affect the pressure results, as the data of Figs. 4 and 5 are averages over many forces.

### 4.3 Force Distribution

We now consider the distribution of contact forces for each packing at different area fractions. Like before, we sample the contacts forces at various points up the incline using a window of  $y - \Delta y/2$  and  $y + \Delta y/2$ . However, we need many contacts to obtain a good distribution of contact forces, and therefore, we use  $\Delta y = 30r_0$ . (Over this range of  $\Delta y$  and for droplets at least 10 diameters up the incline,  $\Delta\phi = (\partial\phi/\partial y)\Delta y = 0.025$ .) This window size gives roughly 2500 contacts for each  $y$  sampled. In Fig. 6(a), the lines show the distribution of contact forces normalized by the mean contact force at locations with  $\phi - \phi_c$  as indicated; all the data are for the  $\sigma = 1.25$  packing. In all our data most forces are near or less than the mean force  $\langle f \rangle$  and that the maximum force is about  $3\langle f \rangle$ , with a somewhat exponential tail. The shape and magnitude of all the curves are roughly the same. All curves show a dip at small forces. The symbols in Fig. 6(a) show the distribution of normal forces from Majmudar *et al.*<sup>14</sup>, an experiment using frictional 2D photoelastic disks. In their experiment, the particles were isotropically compressed to an area fraction  $\sim 0.016$  above the critical area fraction. Our results look essentially the same as theirs, despite the differences in experimental systems. These distributions are also similar to simulations and experiments on 2D and 3D frictionless systems on foams and emulsions<sup>7,11,15,19</sup>. This suggest that the distribution of forces is a fairly universal property of all jammed systems. The shape of our measured distribution is also in general agreement with the predictions of the force network ensemble<sup>29</sup> and is also in agreement with the earlier q-model<sup>24</sup>, although our data are not clear enough to distinguish between these two models.

As observed by Katgert *et al.*<sup>11</sup>, our force distributions slightly narrow with increasing area fraction in Fig. 6(a). To quantify this, we plot the standard deviation of each force distribution in Fig. 6(b). For the  $\sigma = 1.25$  and  $\sigma = 1.42$  packings, the width of the force distributions decreases quickly above the jamming point and then saturates to a constant width of  $\sim 0.5$ . The  $\sigma = 1.52$  packing has a broader distribution of forces at larger  $\phi - \phi_c$  compared to the other two packings, and the decrease in the width as  $\phi - \phi_c$  increases is more subtle. Overall, our results are qualitatively in agreement with<sup>11</sup>, although they did not compute the standard deviations. It is possible that measurement errors in our forces have a dependence on  $\phi$ , as discussed in the Appendix, and that this could affect the dependence of the standard deviation on  $\phi$ . However, the errors are no worse than 16%, much less than the width of the distributions for any  $\phi$ , and so a possible  $\phi$ -dependence of the errors cannot account for the decrease in width seen in Fig. 6(b).

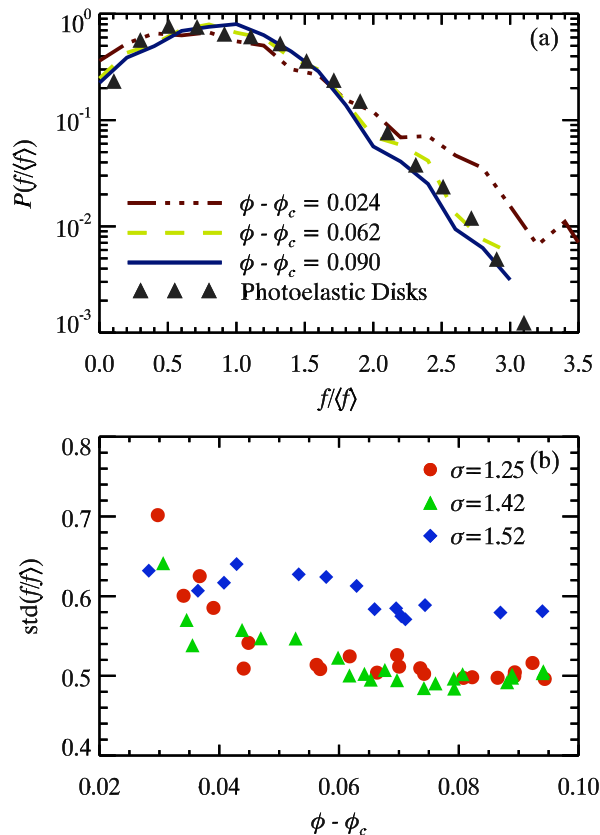


**Fig. 6** (Color online) (a) Distribution of contact forces relative to the mean contact force at different  $\phi$  for the  $\sigma = 1.25$  packing. The mean force is  $\langle f \rangle = 0.011 \mu\text{N}$ ,  $0.045 \mu\text{N}$ , and  $0.13 \mu\text{N}$  for the  $\phi - \phi_c = 0.024, 0.062$ , and  $0.106$  data respectively. The solid triangles are data from a 2D photoelastic disk experiment at  $\phi - \phi_c \sim 0.016$  from Majmudar *et al.*<sup>14</sup>. (b) The standard deviation of  $P(f/\langle f \rangle)$  for each packing at different  $\phi$ . The standard deviation of the Majmudar *et al.* data is 0.52.

### 4.4 Force Chains

In this section we consider various statistical measurements on the randomness of the force chain network, and then we compare predictions of the Brujić-Zhou model<sup>15,19,20,32</sup> to our data. When analyzing data in this section we consider all droplets and contacts between  $40 \leq y/2r_0 \leq 80$ , and over this range  $\phi$  increases from 0.93 to 0.96. We find that all of the properties discussed below do not depend on  $\phi$  at larger area fractions, and so considering this larger range of  $\phi$  gives us better statistics.

To start, we define a force segment to belong to a force chain if it is one of the two largest forces on both droplets joined by the force segment. Under this definition, each droplet can only have a maximum of two force segments that belong to a force chain, and therefore, our definition does not allow for force

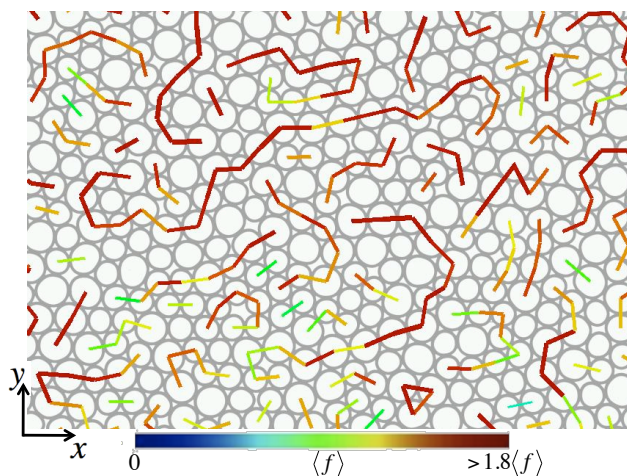


**Fig. 7** (Color online). This image shows only the forces belonging to a force chain within a region of the  $\sigma = 1.25$  sample. On average, the forces are larger further up the image because the sample is inclined, and this can be observed in the image by the increasing redness of the force segments at the top.

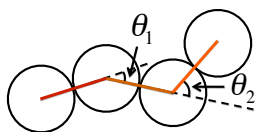


**Fig. 8** (Color online). Definitions of the angles  $\theta_1$  and  $\theta_2$  between joining force segment. In the sketch both  $\theta_1$  (clockwise to extended line) and  $\theta_2$  (counter clockwise to extended line) are positive. If there is a correlation in orientation that tends to make force chains linear, then the correlation between  $\theta_1$  and  $\theta_2$  is positive.

chain branching or merging, which will simplify the analysis below. Note that even droplets with small forces can participate in force chains, given that the definition only requires the force segments to be large for the given droplet and its contacting neighbors. Figure 7 shows force chains using our definition. These chains are fairly linear and vary in length from 1 to more than 10 force segments. Our samples are formed by slow compaction due to buoyant forces, which may introduce an anisotropy in the force chain network<sup>14,23,41</sup>. Indeed, we find a slight bias for force chain segments to be orientated up the incline.

Given that force chains form linear like structures and that there is a slight anisotropy for force chains to align along the incline we may expect there to be correlations in the orientation of neighboring force chain segments. To quantify such a correlation we define two relative angles  $\theta_1$  and  $\theta_2$  between joining force segments, where the definition of  $\theta_1$  and  $\theta_2$  are shown in Fig. 8. We compute the Pearson correlation coefficient  $C = \text{cov}(\theta_1, \theta_2) / \sigma_\theta^2$ , where  $\text{cov}(\theta_1, \theta_2)$  is the covariance

of  $\theta_1$  and  $\theta_2$  and  $\sigma_\theta$  is the standard deviation of  $\theta$ . We find that for all  $\phi$ ,  $C$  is zero or nearly zero (at most  $C = 0.2$ ), indicating no correlation. This agrees with prior work on 3D emulsions<sup>15,19</sup>. Thus, the apparent linearity of force chains seen in some locations of Fig. 7 is not due to correlations in the relative direction of neighboring segments that would keep the chain straight.

To further explore the tendency for force chains to be linear, we consider the distribution of  $\theta_1$ , where we drop the subscript 1 as we are only focusing on two force segments at a time rather than three. In Fig. 9(a) we plot the distribution in  $\theta$  for all three packings. The distribution shows that most force chain segments form at an angle  $|\theta| < 60^\circ$ . Thus, force segments tend to form a linear chain not because their orientations are correlated, but simply because it's more probable that they are oriented at small angles relative to each other. Using our  $P(\theta)$  data, we determine the persistence lengths  $l$  using the standard definition of persistence length for polymer chains.

We find  $l = 4.4\langle r_0 \rangle$ ,  $4.8\langle r_0 \rangle$ , and  $3.8\langle r_0 \rangle$  for the  $\sigma = 1.25, 1.42$ , and  $1.52$  data. These are the distances beyond which the force chain has “forgotten” its original direction. In analyzing the distributions similar to  $P(\theta)$  for 3D emulsions, Zhou *et al.*<sup>32</sup> found a persistence length slight larger around  $l \sim 6 - 8\langle r_0 \rangle$ .

To further consider the orientations of force segments in force chains, we consider a model proposed by Brujić *et al.*<sup>19,20</sup> and extended by Zhou *et al.*<sup>15,32</sup>. The Brujić-Zhou model is a method for generating ensembles of local particle configurations (a central particle and contacting first neighbors) and the forces acting on a central particle by its first neighbors. Each local configuration is generated by randomly placing  $z_i$  contacting neighbors such that any two neighboring particles do not overlap. Next, the contact forces between the central particle and  $z_i - 2$  neighboring particles are chosen at random from a distribution  $P(f)$ , leaving two unknown contact forces. We choose  $P(f)$  to match our experimentally measured distributions (see Fig. 6). By invoking force balance, the two remaining contact forces are found algebraically. Once a sufficient number of local configurations are generated, the distribution of force chain orientations can be studied. The basic assumptions of this model are force balance, randomness in the magnitude of forces, and randomness in the orientation of forces. For our data the first assumption applies because the system is in mechanical equilibrium and above we have shown that the other two assumption reasonably apply.

One issue in using the Brujić-Zhou model to predict  $P(\theta)$  is that the model only gives the forces between a central droplet and its first neighbors. To define a force chain segment we also need to know all the forces acting on each first neighbor as well. We therefore extend their model by generating additional forces on the neighboring droplets in exactly the

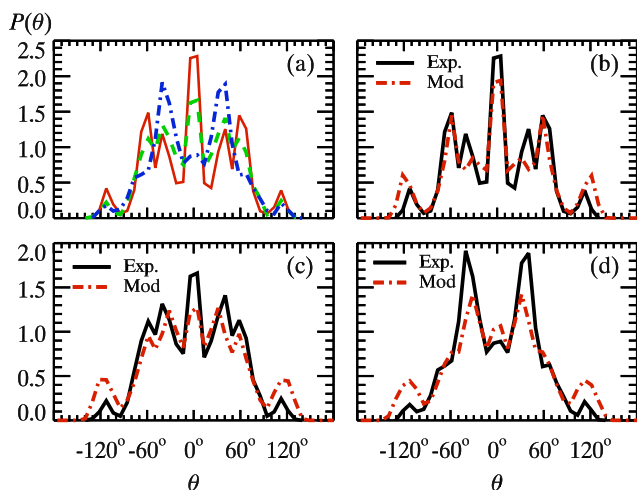


**Fig. 9** (Color online) (a) Distribution of  $\theta$  for each packing, where both  $\theta_1$  and  $\theta_2$  are treated as a single variable  $\theta$ . The red solid line is the distribution for the  $\sigma = 1.25$  packing, the green dashed line is the distribution for the  $\sigma = 1.42$  packing, and the blue dashed-dot line is the distribution for the  $\sigma = 1.52$  packing. (b-d) Comparisons between the experimental distributions and the predictions of the Brujić-Zhou model, for size ratios (b)  $\sigma = 1.25$ , (c)  $\sigma = 1.42$ , and (d)  $\sigma = 1.52$ .

same way (constrained by the forces already chosen for the central droplet). This lets us apply our force chain definition given above, which requires that force segments be among the largest two forces on both droplets the force acts between. We repeat this extended Brujić-Zhou algorithm many times to compile data from all cases where the algorithm gives an instance of two valid force segments so that we can determine  $\theta_1$ . To make the inputs into the model as consistent as possible with our experimental data, instead of randomly generating local configurations, we randomly select local configurations from our experimental data.

Figure 9(b)-(d) compares  $P(\theta)$  measured in our experiments (black solid curves) with the predictions of the model (red dot-dashed curves). The model is in good agreement with the experiment, with the exception of some discrepancies in the magnitudes of the peaks. The model captures significant features of the data: for instance, the peak around  $\theta = 0^\circ$  is much different between Fig. 9(b) and Fig. 9(d), and the model replicates this difference. We also note that if we loosen the definition of force chain segments to simply those forces that are the largest two forces acting on any droplet (independent of how large they are relative to forces on neighboring droplets), we find nearly identical distributions as the ones shown in Fig. 9.

Our analysis suggests so far that the force chain network is random, without long-range correlations. It therefore seems plausible that the distribution of force chain lengths should

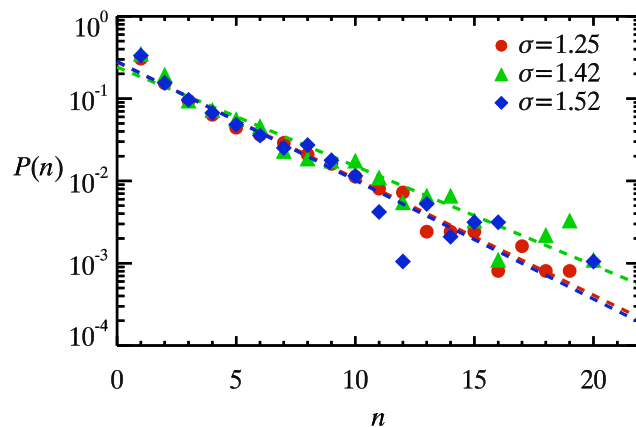


**Fig. 10** (Color online) Distribution of the number of force segments making up distinct force chains. The data points are experimental values and the dashed lines are fits to the data of the form  $P(n) = (1 - p)p^n$ , where  $p$  is found to be 0.722, 0.758, and 0.717 for the  $\sigma = 1.25$ , 1.42, and 1.52 packings, respectively.

obey a random process. If there is a probability  $p$  for a force chain segment to be connected to a neighboring force chain segment, then the distribution of chain lengths should obey the scaling  $P(n) = (1 - p)p^n$ , where  $n$  is the number of force segments within a force chain. In Fig. 10 we plot the distribution of chain lengths for each packing. The data decay exponentially over 3 orders of magnitude. The data are fit by  $P(n) = (1 - p)p^n$  with  $p \approx 0.73$  (see caption for details), indicating that it is highly likely that for a force chain to propagate through the material. The fits are shown as the dashed lines and show good agreement with the data other than at  $n = 1$ .

In granular quasi-static intruder simulations with friction between particles by Peters *et al.*, using a more sophisticated definition of force chains, they also found an exponential distribution of chain lengths<sup>42</sup>. From their reported data on  $P(n)$ , we estimate a value of  $p = 0.65$ . It appears that statistically a force chain can be thought of as a random process with probability  $p$  for the force chain to propagate, independent of  $\phi$  but perhaps depending on the sample details.

## 5 Conclusions

We have introduced a new experimental model system composed of quasi-2D emulsions droplets to study the jamming transition. Our droplets are circular in shape and deform when press into one another, and at the contacts between two droplets the forces are in-plane mimicking a true 2D system. We can accurately measure the forces between touching droplets to within 8%, where our method is not limited to our experiment, and could be extended to determine forces in 2D foams, 3D emulsions, and 3D foams. Our model system has



unique strengths; we can easily make samples with any distribution in particle sizes, emulsions are stable over many days, setup is cheap, our droplets have no static friction, and our method can be extended to cases of flow<sup>43</sup>.

Using our model system we observed power-law scaling of the contact number and pressure with  $\phi - \phi_c$ , similar to prior numerical models<sup>5–8</sup>. Notably we find that all three fit parameters for the contact number scaling are quite close to the values found in 2D simulations. We verify experimentally for the first time a link between the interparticle force law and the critical pressure exponent, illustrating a direct relationship between the bulk properties of an amorphous solid and the interaction between the constituent particles. The agreement of our results and the numerical models shows that the qualitatively different particle interaction we have does not play a significant role in determining the geometric structure and bulk modulus.

Our analysis of the inter-particle forces found a probability distribution of forces in good agreement with those found in prior experiments and simulations, strongly suggesting that the shape is universal. We further examined the spatial structure of the large forces (“force chains”). The directions of neighboring force chain segments are uncorrelated although there is a tendency for two force chains to be in the same direction. This is a sensible result as this allows the large forces acting on a droplet to balance one another. The Brujić-Zhou model, which assumes random and uncorrelated force segments, recovers our experimentally observed probability distribution of angles between adjacent force segments.

This work provides more evidence for the universality of various properties of the jamming transition, such as critical scaling, the shape of the force distribution, and the structure of the force network.

## Acknowledgments

We thank G. Hunter and G. Hentschel for helpful discussions. This work was supported by the donors of The Petroleum Research Fund, administered by the American Chemical Society (grant 47970-AC9), and additionally by the National Science Foundation (grant CBET-0853837).

## A Method For Determining Force Law

In this section we describe in detail our method for determining an empirical force law that relates the outline of droplets to the contact forces. For an overview of our method see Sec. 3. This section is organized in the following manner: first, we discuss the measurements from droplet outlines; second, we discuss the general form of possible force laws; third,

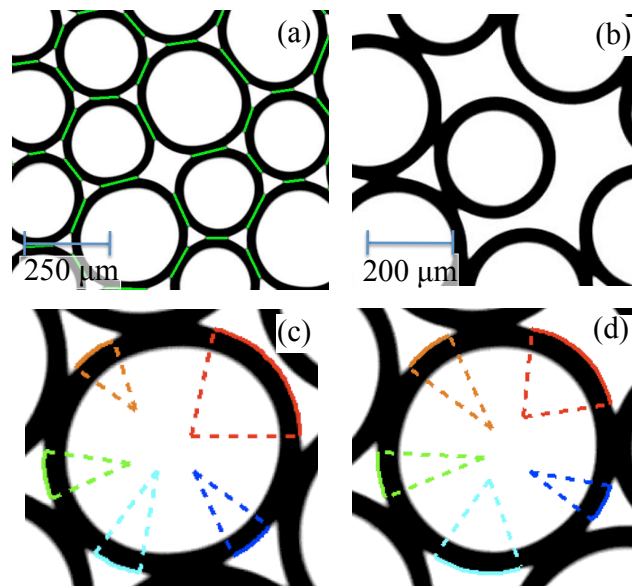


**Fig. 11** (Color online). (a) Experimental image of droplets with the contacts found using our algorithm indicated by green lines. (b) Experimental image of a droplet being held in contact with two neighboring droplets due to a slight adhesion. In this image the droplets are motionless and the system is not inclined. (c, d) A close up view of a droplet. Each portion of the water-oil interface is fitted to an arc with constant radius of curvature. The fits are shown as the different colored arcs.

we present the optimization problem; fourth, we deduce the best force law consistent with the data.

### A.1 Measurable Variables

In this subsection, we discuss the various quantities measurable from droplet images, and their measurement errors. In the following subsections, these quantities will be used to determine the forces between droplet pairs.

The larger the contact between two droplets, the more force they feel. This is quantified by the contact length  $l_{ij}$  between two droplets. We measure this by identifying the portion of each droplet’s perimeter that is shared between them, shown as the light green lines in Fig. 11(a).  $l_{ij}$  is calculated as the length of the line segment. Since we can only measure the two endpoints of each contact to 1 pixel accuracy, we have an uncertainty  $\delta l$  of  $\sqrt{2}$  pixels. For our highest magnification lens ( $5\times$ ) this gives  $\delta l = 1.1 \mu\text{m}$  and for our lower magnification lens ( $1.6\times$ ) this gives  $\delta l = 1.96 \mu\text{m}$ .

One expects that any two droplets with a nonzero contact length ( $l_{ij} > 0$ ) would experience a repulsive force at the contact. However, we observe a slight attractive interaction between droplets as shown in Fig. 11(b), where the central droplet is adhering to two neighboring droplets. In this par-

ticular configuration, the adhesion force is balanced by the repulsive force, and therefore, the net force at each contact on the central droplet is zero for some finite contact length  $l_0$ .

We determine  $l_0$  by averaging together the contact lengths found between 25-50 droplets at the very bottom of the incline. The standard deviation of these contact lengths is about  $0.025r_0$ , which is one to two orders of magnitude smaller than measured contact lengths  $l_{ij}$  of deformed droplets in contact, and therefore we conclude that  $l_0$  is reasonably well-defined by the mean value. In addition to the adhesion, some of the finite contact length is due to optical resolution limits resulting in a systematic effect: for similar conditions,  $l_0$  is shorter when using the  $1.6\times$  lens (data in Table 3) as compared to the  $5\times$  lens (data in Table 4). Accordingly, the force law will be taken to depend on  $\Delta l = l - l_0$ , canceling the systematic effect, and the force law will be required to obey  $f(\Delta l = 0) = 0$ . We could also require  $f(l) - f(l_0)$ , but this will not produce force laws of any better quality and often the force laws will be more complex in form.

Near the jamming area fraction, our fractional uncertainty is typically  $\delta l/\Delta l_{ij} \approx 100\%$ . In contrast, ten droplet diameters up the incline ( $\phi - \phi_c \approx 0.01$ ) typical values of  $\Delta l_{ij}$  are much larger and the uncertainty drops to about  $\delta l/\Delta l_{ij} \approx 5\%$ , and decreases further still for larger  $\phi$ .

Next, we wish to know the curvature of the droplet outline. We measure  $r_i$  for a droplet by locating each portion of the perimeter belonging to a water-oil interface, that is, not touching another droplet. We fit these portions of the interface to an arc of constant curvature as shown in Fig. 11(c,d) to obtain a local radius of curvature for each portion. The radii for the different portions should be the same, but in practice they vary due to noise. We arithmetically average these local radii of curvature to obtain the mean curvature  $r_i$  for the droplet. To determine the uncertainty, we create artificial images of circular perimeters with known radii and noise commensurate to our experimental data, and fit these perimeters to find values of  $r$ . The distributions of  $r$  reproduce the experimentally observed variance in the individual radii of curvature, and let us deduce that the measurement error of  $r_i$  is 3.5% for the  $5\times$  lens and 7% for the  $1.6\times$  lens. In contrast to  $\Delta l$  which is easier to measure at large  $\phi$ ,  $r_c$  is harder to measure at large  $\phi$  as the curved portions of droplets are shorter. Closer to  $\phi_c$ , these uncertainties are smaller.

The last measurable quantity to consider is  $\bar{R}$ , the mean 3D curvature of a compressed emulsion droplet in our quasi-2D system. This curvature relates to the Laplace pressure and so may be relevant for the force law, although we will show below that it is not needed; nonetheless we discuss it for completeness. For scenarios where droplets are asymmetrically deformed in 3D, the water-oil interface has two principle radii, the maximum radius of curvature  $R_{i,1}$  and the minimum radius of curvature  $R_{i,2}$ . For droplets compressed in this manner, the

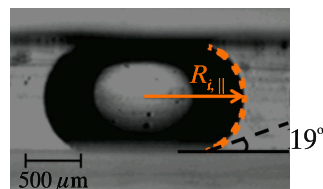


**Fig. 12** (Color online). An experimental image of a mineral oil droplet squeezed between two glass slides, where the gap thickness is 1 mm,  $R_{i,||} = 0.88$  mm and  $R_{i,\perp} = 0.56$  mm. The orange (light) dashed line is a fit to the perimeter to obtain  $R_{i,||}$  and  $R_{i,\perp}$ .

mean curvature  $1/\bar{R}_i = 1/2(1/R_{i,1} + 1/R_{i,2})$  is constant anywhere on the surface.

To measure  $R_{i,1}$  and  $R_{i,2}$  experimentally we take side view images of isolated droplets in a sample chamber of gap thickness  $h = 1$  mm (see Fig. 12). The width of the droplet cross-section is  $2R_{i,1}$ , and corresponds to the droplet radius that would be measured as the 2D radius in the normal top-down view of our experiments. The free surface of this compressed droplet is a surface of mean curvature  $\bar{R}$ ; this is not a circular arc of constant radius as  $R_1$  varies with height. To obtain  $R_{i,1}$  and  $R_{i,2}$  of the droplet, we fit the surface using the method of Caboussat and Glowinski<sup>44</sup> (an algorithm to generate the surface of a droplet compressed between two boundaries). In Fig. 12, we show the fit as the orange dashed line. Repeating this method for many droplets, we find  $R_{i,\perp}/h = 0.552 \pm 0.011$  for droplets in the size range we use. For simplicity, we simply use  $R_{i,\perp} = 0.552h$  for all  $r_i$ .

## A.2 Mathematical Treatment of an Empirical Force Law

Our goal is to find an empirical force law  $f(l_{ij}, l_0, r_i, r_j)$  relating the contact force between two droplets  $i$  and  $j$  to the information about their outlines. *A priori* it is useful to consider what such a force law should look like.

We first consider two cases where the force law is already known, the ideal 2D case and the ideal 3D case. By ideal, we mean that the contact angle between two droplets is zero, and where there are no adhesive forces. Generally these are not realistic assumptions, due to the interactions between the surfactant molecules at the contacting interface<sup>45,46</sup>. For the ideal cases, the force between two droplets in contact can be modeled using Princen's 2D model<sup>47-49</sup> or Zhou's 3D model<sup>50</sup>. We use lower case to indicate 2D variables and upper case to indicate 3D variables. In 2D, the contact between two droplets has a contact length  $l_{ij}$ , and in 3D, the contact has contact area  $A_{ij}$ . The force law for the two models are

$$\text{2D Model: } f_{ij} = \gamma_{2D} \frac{l_{ij}}{r_{ij}}, \text{ where } r_{ij} = \frac{r_i + r_j}{r_i r_j} \quad (2)$$

$$3D \text{ Model: } F_{ij} = \gamma_{3D} \frac{A_{ij}}{R_{ij}}, \text{ where } R_{ij} = \frac{R_i + R_j}{R_i R_j} \quad (3)$$

In the above equations,  $\gamma_{2D}$  is a 2D line tension and  $\gamma_{3D}$  is a 3D surface tension. For scenarios where droplets are asymmetrically deformed in 3D, the radius of curvature  $R_{ij}$  in the 3D model must be replaced by the mean curvature  $\bar{R}_{ij}$ .

The 2D model would be straightforward to apply as we directly measure  $l_{ij}$ ,  $r_i$ , and  $r_j$ . To apply the 3D model, a reasonable assumption is that  $A_{ij}$  is related to  $l_{ij}$  and perhaps the droplet radii. The radii  $\bar{R}_i$  and  $\bar{R}_j$  are measurable as described in the previous subsection.

Rather than choosing between the 2D and 3D models, we test generalizations of both models and let the data select what works best. As described above, one of our variables the force will depend on is  $\Delta l_{ij}$  and we constrain all possible force laws so that  $f(\Delta l_{ij} = 0) = 0$ . In general, we consider models of the form  $f_{ij}^{(2D)}(\Delta l_{ij}, 1/r_{ij}; \vec{\alpha})$  for 2D and  $f_{ij}^{(3D)}(\Delta l_{ij}, 1/\bar{R}_{ij}; \vec{\alpha})$  for 3D.  $\vec{\alpha} = \alpha_1, \alpha_2, \dots$  are the fitting parameters associated with a given functional form. To give an example, we could write  $f_{ij}^{2D} = \alpha_1 (\Delta l_{ij}/r_{ij})^{\alpha_2}$  with fitting parameters  $\alpha_1$  and  $\alpha_2$ . In all, we test a total of 86 various 2D and 3D force laws of different functional forms that include exponentials, hertzians, power laws, and polynomials in  $l_{ij}$ ,  $1/r_{ij}$ , and  $1/\bar{R}_{ij}$ , and combinations of these forms.

### A.3 Optimization Problem

To test the force laws, we establish constraints from the data, optimize each force law subject to the constraints, and then quantify how well the optimum force laws describe the data. To start with, we consider the constraints on forces in the  $x$  and  $y$  directions.

In the  $y$ -direction the sum of the forces on any given droplet is equal to the buoyant weight  $W_D$ . This is in practice hard to use directly, as  $W_D$  is small compared to the contact forces, and likely below limits set by noise. Therefore, rather than considering individual droplets, we note that droplets located at a given  $y$  must support the observed total buoyant weight  $W_{obs}$  of droplets below them, known simply from measuring the total area of droplets with centers below  $y$ . The way in which these droplets support this buoyant weight is through contact forces, and for an assumed force law  $f_{ij}(\Delta l_{ij}, 1/r_{ij}; \vec{\alpha})$  we can determine these contact forces by substituting our measured values for  $\Delta l_{ij}$  and  $r_{ij}$  (or  $\bar{R}_{ij}$ ) into the function. If the assumed force model accurately predicts the forces, then the sum of these contact forces  $\sum F_{mod,y}$  at a given  $y$  will equal  $W_{obs}$ . Here  $\sum F_{mod,y}$  are the sum of the  $y$ -component of only those forces pointed in the downward directions. The reason we only consider the downward facing forces is because the collective buoyant weight is pushing upward, and to satisfy Newton's 3rd law, the balancing forces must be facing downward. We convert  $W_{obs}$  and  $F_{mod,y}$  into 2D pressures (force per

unit length) by writing  $\lambda_{obs} = W_{obs}/w$ ,  $\lambda_{mod} = \sum F_{mod,y}/w$ , using the width of the chamber  $w$ .  $\lambda$  is in essence the 2D hydrostatic pressure at height  $y$ . Because there is no static friction at the sidewalls, there is no Janssen effect<sup>51</sup>.

We define a goodness of comparison in the  $y$ -direction as

$$\chi_y^2 = \sum_y [(\lambda(y)_{obs} - \lambda(y)_{mod}) / \langle \lambda(y)_{obs} \rangle]^2, \quad (4)$$

where smaller values of  $\chi_y^2$  indicate a better match between the assumed force law and the actual forces. In the equation,  $y$  indexes various distances up the incline where  $\lambda(y)_{mod}$  and  $\lambda(y)_{obs}$  are sampled, and the angle brackets are an average over  $y$ . We normalize by  $\langle \lambda(y)_{obs} \rangle$  to make  $\chi_y^2$  dimensionless, and since  $\langle \lambda(y)_{obs} \rangle$  is independent of the assumed force law, it does not change the results. We sample  $\lambda$  at intervals of  $5r_0$  up the incline. At each  $y$  sampled,  $\lambda_{mod}$  is calculated using the contact lengths and droplet radii for all droplets found between a distance  $y - 5r_0$  and  $y + 5r_0$  up the incline, and  $\lambda_{obs}$  is calculated using the position and radii of all droplets below a distance  $y$  up the incline.

We next consider the forces in the  $x$ -direction. In contrast to the  $y$ -direction there are no external forces, so the sum of the forces on each droplet in the  $x$ -direction is zero. From this we construct the goodness of comparison

$$\chi_x^2 = \sum_i \left[ \left( \sum_j f_{x,ij} \right) / \langle |\vec{f}_i| \rangle \right]^2, \quad (5)$$

where the  $F_{x,ij}$  is the  $x$  component of the force at a contact between droplets  $i$  and  $j$  and  $\langle |\vec{f}_i| \rangle$  is the average net contact force exerted on droplet  $i$ . In the equation,  $f_{x,ij}$  are the forces predicted by the assumed force law. Due to measurement error, the forces will not sum to zero, and the deviation from zero grows with  $\langle |\vec{f}_i| \rangle$ . We assume that the deviation will grow linearly with  $\langle |\vec{f}_i| \rangle$  and to fairly weight the contributions of each droplet to  $\chi_x^2$ , we normalize the sum of the forces by  $\langle |\vec{f}_i| \rangle$ .

Finally, we define a net goodness of comparison  $\chi^2 = \chi_x^2 \chi_y^2$  which indicates how well an assumed force law models the forces in both the  $x$  and  $y$  directions. Since we know the buoyant weight of our droplets in units of  $\mu\text{N}$ , this allows us to find a force law in units of  $\mu\text{N}$ . Later, we compare  $\chi^2$  between the different force laws to determine the best overall force law.

### A.4 Empirical Force Law: Monodisperse and Bidisperse

We now apply our method to find an empirical force law. We start by determining the force law for same size droplets in contact using data taken on four different monodisperse samples. The samples are prepared by placing droplets with 3D radius  $R_0$  into a sample chamber with gap thickness either  $100 \pm 4 \mu\text{m}$  or  $180 \pm 4 \mu\text{m}$ , and once in the chamber, the droplets have a 2D radius of  $r_0$ . The error assigned in the

$R_0$ [ $\mu\text{m}$ ]	$r_0$ [ $\mu\text{m}$ ]	$h$ [ $\mu\text{m}$ ]	poly (%)	$l_0$ [ $\mu\text{m}$ ]
164	183	186	5.5	50.8
143	156	180	1.6	48.8
105	128	96	1.9	36.6
84.1	89	96	2.5	30.3

**Table 3** Parameters characterizing the droplets in our 4 different monodisperse samples.  $R_0$  is the 3D radius of the droplets,  $r_0$  is the 2D radius,  $h$  is the gap thickness of the chamber, poly is the polydispersity of the sample, and  $l_0$  is the length of contact for two droplets just in contact. Our uncertainties for the various measures are  $\pm 0.2 \mu\text{m}$  in  $R_0$ ,  $\pm 2 \mu\text{m}$  in  $r_0$ , and  $\pm 4 \mu\text{m}$  in  $h$ . The variability in  $l_0$  grows with droplet size and the measurement uncertainty can be expressed as  $\pm 0.04r_0$  in  $l_0$ .

gap thickness represents the unavoidable variations in the gap thickness measured at different points along the sample chamber. We note that the larger the sample chamber, the larger the variability of gap thickness we observe. As the chambers are inexpensive, sample chambers with more variability than  $\pm 4 \mu\text{m}$  are discarded. After the sample chambers are filled, they are sealed to prevent evaporation, and then placed on a microscope inclined at  $28^\circ$ . Droplets rise to the top and come to rest in mechanical equilibrium, at which point we acquire images of the sample. Various parameters characterizing each monodisperse sample are shown in Table 3.

To determine the best force law we pick each possible functional form, optimize the parameters  $\bar{\alpha}$  for it, and then compare  $\chi^2$  for the different functions. Several functional forms all have small  $\chi^2$  values, and of these we choose one that is simple and plausible. For simplicity, measuring the 2D  $r_{ij}$  is simpler than measuring the 3D  $\bar{R}_{ij}$ . For plausibility, functions that treat  $\Delta l_{ij}$  and  $r_{ij}$  as  $\Delta l_{ij}/r_{ij}$  most closely resemble Eqn. 3.

We judge the most reasonable function with low  $\chi^2$  to be  $F_{ij} = \alpha_1 \Delta l_{ij}/r_{ij} + \alpha_2 (\Delta l_{ij}/r_{ij})^2$ , quite similar to Eqn. 3. We also choose this function because we find that we can easily rescale this function using the 3D droplet radius  $R_0$  so that we have a universal force law for all four data sets (the four different droplet sizes). The rescaled force law is

$$F_{ij} = \alpha_1 R_0 \Delta l_{ij}/r_{ij} + \alpha_2 (R_0 \Delta l_{ij}/r_{ij})^2. \quad (6)$$

where  $\alpha_1 = 4.25 \mu\text{N}/\text{mm}$  and  $\alpha_2 = 4.12 \mu\text{N}/\text{mm}^2$ .

The rescaled force law is shown for each data set in Fig. 13. We see that all the force laws are nearly linear; the quadratic correction is about 10% for the largest forces. The rescaled force law shows that all the data collapse very well and only slightly deviate between each other at larger  $\Delta l_{ij}/r_{ij}$ . For these larger values in  $\Delta l_{ij}/r_{ij}$ , the area fraction is close to 0.96 which is the upper limit where we can still confidently measure  $r_{ij}$ ; for those close-packed droplets, only a few pixels occupy the water-oil interface and  $r_{ij}$  is hard to determine. We do not

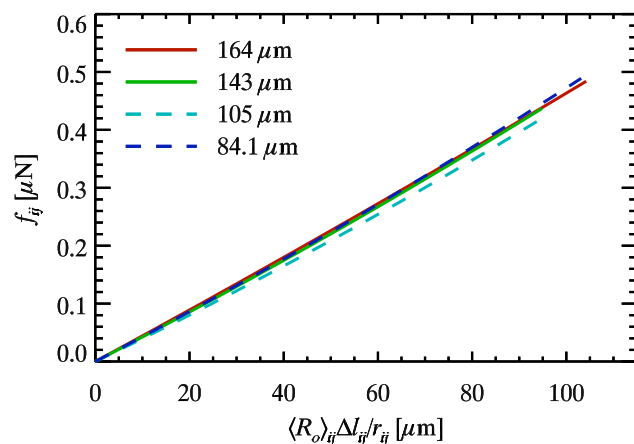


**Fig. 13** (Color online). A plot of the universal empirical force law for each data set. The solid lines are samples with a gap thickness of approximately  $180 \mu\text{m}$  and the dashed lines are samples with a gap thickness of approximately  $110 \mu\text{m}$ . The legend indicates  $R_0$ .

claim that Eqn. 6 is the correct force law; in particular, while  $\alpha_1$  has units of surface tension and is plausible for an oil-water surface tension, the physical meaning of  $\alpha_2$  is unclear. Rather, Eqn. 6 accurately provides the forces between our droplets, within the measurement limitations set by our data. Also, there may be other sources of error, for instance, Lacasse *et al.*<sup>52</sup> has numerically shown that the force law has a slight sensitivity to the number of neighbors and the relative positioning of the neighboring droplets. To examine if there are other potential sources of error, using Eqn. 6 we compared the deviations in the computed net force on each droplet to the deviations we expect given our measurement errors, and find the two agree well. Thus, within the limitations of our measurement errors, we have resolved the forces as best as possible, confirming Eqn. 6 is adequate.

To test how well one can determine a force law given finite data and measure error, we additionally simulated inclined mechanically stable droplet packings of 1000 droplets with a known force law, then added noise to the data consistent with experimental noise. Applying our empirical method to the simulated data, we recover the known force law with 2% errors in the coefficients (noise equivalent to the experiments using the  $5\times$  microscope objective) or 5% errors in the coefficients (noise equivalent to the experiments with the  $1.6\times$  microscope objective). This suggests it is possible that the  $\sim 4\%$  variations between the force laws for different sized droplets seen in Fig. 13 are simply due to noise, and they may well have exactly the same force law.

So far we have focused on force laws in monodisperse samples, but we also need to measure forces between different-sized droplets in bidisperse samples. To obtain a force law between droplets of different sizes, we apply our method to



$\sigma$	$R_0^{(big)}$ [ $\mu\text{m}$ ]	$R_0^{(small)}$ [ $\mu\text{m}$ ]	$h$ [ $\mu\text{m}$ ]	$l_0^{(ss)}$ [ $\mu\text{m}$ ]	$l_0^{(sb)}$ [ $\mu\text{m}$ ]	$l_0^{(bb)}$ [ $\mu\text{m}$ ]
1.25	102	86.5	104	52.0	56.0	63.0
1.42	91.8	80.0	106	46.8	50.9	58.5
1.52	108	79.2	104	45.0	51.0	58.7

**Table 4** The parameters characterizing the droplets in our 3 bidisperse samples. Other parameters related to these droplets are shown in Table 1. The first column  $\sigma = r_0^{(big)}/r_0^{(small)}$  is the size ratio. The two radii shown are the 3D droplet radii of the small and big droplets before placing them in the chamber. There are also three contact types: small-small (*ss*), small-big (*sb*), and big-big (*bb*), and therefore there are three  $l_0$  values. Our uncertainties for the various measures are  $\pm 0.2 \mu\text{m}$  in  $R_0$  and  $\pm 4 \mu\text{m}$  in  $h$ . The variability in  $l_0$  grows with droplet size and the measurement uncertainty can be expressed as  $\pm 0.04r_0$ .

find an empirical force law using data taken on three different bidisperse samples. The bidisperse samples are prepared in the same manner as the monodisperse case. Table 4 summarizes the various parameters of our bidisperse systems; see also Table 1.

For the case of a bidisperse sample with small and big droplets, there are 3 possible contact types to consider: small-small, small-big, and big-big. Our previous results give us small-small and big-big forces. We assume the unknown small-big force law obeys the same functional form as the monodisperse case (Eqn. 6), where  $\alpha_1$  and  $\alpha_2$  need to be determined. Recall that Eqn. 6 contains a term  $R_0$  that rescales the force law and makes it universal. For the small-big contacts there are two different  $R_0$  values, one for each droplet size. To account for these two radii we substitute  $R_0$  with the arithmetic mean of the two radii  $\langle R_0 \rangle$  giving us our bidisperse empirical force law  $F_{ij} = \alpha_1 \langle R_0 \rangle \Delta l_{ij} / r_{ij} + \alpha_2 (\langle R_0 \rangle \Delta l_{ij} / r_{ij})^2$ , where  $\alpha_1$  and  $\alpha_2$  are unknown. To obtain  $\alpha_1$  and  $\alpha_2$  for our bidisperse samples we minimize  $\chi_x^2$ , and find that  $\alpha_1$  and  $\alpha_2$  are very close to that found for the monodisperse case and within the 4% variation we expect from due to finite sampling and measurement error. Therefore, we have shown that to within 5% error we have found a universal force law that works for any droplet size and is close to Princen's 2D model<sup>47–49</sup> with a small second order correction.

### A.5 Final comments on force law

The uncertainties in determining forces are related to the magnification. The higher the magnification, the better we can measure the contact length  $l$  and the mean curvature  $r$ . Fortunately, given that we study static samples, this means we can take overlapping images at high magnification to reduce our uncertainties, as described in Sec. 2. In an experiment

with moving droplets, overlapping images of different fields of view would be difficult or impossible. This situation would require limiting the field of view to fewer droplets, if the same resolution of forces was desired. For any magnification, uniformity of lighting is essential so that the appearance of droplets is uniformly related to their true shape and size. As discussed in the previous subsection, our imperfect knowledge of the force law gives us a systematic uncertainty no worse than 5%. To determine the random uncertainty for particular forces, we take measured  $r_{ij}$  and  $\Delta l_{ij}$  values, add noise commensurate to our known uncertainty (discussed in Sec. A.1), and recalculate the force to see the variation. The bidisperse data of Sec. 4 were taken with a  $1.6\times$  lens and have a random uncertainty of 16%. The monodisperse data used in the calibration procedure were taken with a  $5\times$  lens and have a random uncertainty of 8%.

An additional experimental complication is that droplets at rest occasionally feel a static force from the top and bottom plates. This is likely due to contact line pinning on impurities or microscopic scratches on the glass. To minimize this, we pre-clean each slide with methanol which we gently blow off the slide. Harsher cleaning methods do not significantly reduce the droplet pinning. The magnitude of these forces can be estimated by examining a dilute concentration of droplets in a horizontal slide, and then slowly tilting the slide to see when the droplets begin to move due to gravity. For the samples discussed in this work, they begin to move at tilt angles of about  $4.5^\circ$  or sooner. We discard any sample chambers with pinning stronger than this. Given that our experiments are conducted at a tilt angle of  $28^\circ$ , the buoyant weight of a droplet is  $\sin(28^\circ)/\sin(4.5^\circ) = 6$  times larger than any pinning force. Taking the analysis a little further, since the friction force on any droplet can range from zero to the maximum, a more appropriate estimate for the buoyant weight of a droplet is  $\sin(28^\circ)/(\sin(4.5^\circ)/2) = 12$  times the average pinning force. These estimates show that the inter-droplet forces seen in the jammed emulsions ( $\phi > \phi_c$ ) are on the order of a hundred times the pinning forces. We believe that the situation in our calibration experiments are even more favorable. After compaction, the pinning forces should be in random directions, as an analogous granular experiment observed that particles move in random directions during compaction<sup>53</sup>. Therefore, a vector average gives a pinning force on each droplet very close to zero. Since our empirical method relies on the average vector forces on a droplet, the pinning forces can safely be neglected in the results of Sec. 4. Note that if our experiment was scaled down in size (smaller droplets, thinner plate gap) the pinning forces become more significant compared to the droplet weight and can dominate the results.

---

## References

- 1 V. Trappe, V. Prasad, L. Cipelletti, P. N. Segre and D. A. Weitz, *Nature*, 2001, **411**, 772–775.
- 2 A. O. N. Siemens and M. van Hecke, *Physica A*, 2010, **389**, 4255–4264.
- 3 M. V. Hecke, *J. Phys.: Cond. Matt.*, 2010, **22**, 033101.
- 4 A. J. Liu and S. R. Nagel, *Ann. Rev. Cond. Mat. Phys.*, 2010, **1**, 347–369.
- 5 D. J. Durian, *Phys. Rev. Lett.*, 1995, **75**, 4780–4783.
- 6 D. J. Durian, *Phys. Rev. E*, 1997, **55**, 1739–1751.
- 7 C. S. O'Hern, S. A. Langer, A. J. Liu and S. R. Nagel, *Phys. Rev. Lett.*, 2002, **88**, 075507.
- 8 C. S. O'Hern, L. E. Silbert, A. J. Liu and S. R. Nagel, *Phys. Rev. E*, 2003, **68**, 011306.
- 9 W. G. Ellenbroek, E. Somfai, M. van Hecke and W. van Saarloos, *Phys. Rev. Lett.*, 2006, **97**, 258001.
- 10 T. S. Majumdar, M. Sperl, S. Luding and R. P. Behringer, *Phys. Rev. Lett.*, 2007, **98**, 058001.
- 11 G. Katgert and M. van Hecke, *Europhys. Lett.*, 2010, 34002.
- 12 Liu, S. R. Nagel, D. A. Schecter, S. N. Coppersmith, S. Majumdar, O. Narayan and T. A. Witten, *Science*, 1995, **269**, 513–515.
- 13 M. E. Cates, J. P. Wittmer, J. P. Bouchaud and P. Claudin, *Chaos*, 1999, **9**, 511–522.
- 14 T. S. Majumdar and R. P. Behringer, *Nature*, 2005, **435**, 1079–1082.
- 15 J. Zhou, S. Long, Q. Wang and A. D. Dinsmore, *Science*, 2006, **312**, 1631–1633.
- 16 D. Howell, R. P. Behringer and C. Veje, *Phys. Rev. Lett.*, 1999, **82**, 5241–5244.
- 17 D. W. Howell, R. P. Behringer and C. T. Veje, *Chaos*, 1999, **9**, 559–572.
- 18 Q.-C. Sun and S.-Y. Ji, *Chinese Phys. Lett.*, 2011, **28**, 064501.
- 19 J. Brujić, S. F. Edwards, D. V. Grinev, I. Hopkinson, D. Brujić and H. A. Makse, *Faraday Disc.*, 2003, **123**, 207–220.
- 20 J. Brujić, S. F. Edwards, I. Hopkinson and H. Makse, *Physica A*, 2003, **327**, 201–212.
- 21 H. M. Jaeger, S. R. Nagel and R. P. Behringer, *Rev. Mod. Phys.*, 1996, **68**, 1259–1273.
- 22 A. Tordesillas, *Philos. Mag.*, 2007, **87**, 4987–5016.
- 23 M. E. Cates, J. P. Wittmer, J. P. Bouchaud and P. Claudin, *Phys. Rev. Lett.*, 1998, **81**, 1841–1844.
- 24 S. N. Coppersmith, C. H. Liu, S. Majumdar, O. Narayan and T. A. Witten, *Phys. Rev. E*, 1996, **53**, 4673–4685.
- 25 M. Otto, J. P. Bouchaud, P. Claudin and J. E. S. Socolar, *Phys. Rev. E*, 2003, **67**, 031302.
- 26 F. Radjai, M. Jean, J. J. Moreau and S. Roux, *Phys. Rev. Lett.*, 1996, **77**, 274–277.
- 27 C. Thornton, *KONA Powder and Particle*, 1997, **15**, 81–90.
- 28 C. S. O'Hern, S. A. Langer, A. J. Liu and S. R. Nagel, *Phys. Rev. Lett.*, 2001, **86**, 111–114.
- 29 J. H. Snoeijer, T. J. H. Vlugt, M. van Hecke and W. van Saarloos, *Phys. Rev. Lett.*, 2004, **92**, 054302.
- 30 S. Henkes, C. S. O'Hern and B. Chakraborty, *Phys. Rev. Lett.*, 2007, **99**, 038002.
- 31 B. P. Tighe, A. R. T. van Eerd and T. J. H. Vlugt, *Phys. Rev. Lett.*, 2008, **100**, 238001.
- 32 J. Zhou and A. D. Dinsmore, *J. Stat. Mech.-Theory E*, 2009, **2009**, L05001.
- 33 B. Chakraborty, *Soft Matter*, 2010, **6**, 2884–2893.
- 34 P. Claudin, J. P. Bouchaud, M. E. Cates and J. P. Wittmer, *Phys. Rev. E*, 1998, **57**, 4441–4457.
- 35 S. Edwards and C. Mounfield, *Physica A*, 1996, **226**, 1–11.
- 36 R. Shah, H. Shum, A. Rowat, D. Lee, J. Agresti, A. Utada, L. Chu, J. Kim, A. Fernandez-Nieves and C. Martinez, *Materials Today*, 2008, **11**, 18–27.
- 37 K. W. Desmond and E. R. Weeks, *Phys. Rev. E*, 2009, **80**, 051305.
- 38 F. Aurenhammer, *SIAM J. Comput.*, 1987, **16**, 78–96.
- 39 A. Okabe, B. Boots, K. Sugihara and S. N. Chiu, *Spatial Tessellations: Concepts and Applications of Voronoi Diagram*, Wiley, 2nd edn, 2000.
- 40 M. P. Allen and D. J. Tildesley, *Computer Simulation of Liquids*, Oxford University Press, USA, 1989.
- 41 M. Toiya, J. Stambaugh and W. Losert, *Phys. Rev. Lett.*, 2004, **93**, 088001.
- 42 J. F. Peters, M. Muthuswamy, J. Wibowo and A. Tordesillas, *Phys. Rev. E*, 2005, **72**, 041307.
- 43 D. Chen, K. W. Desmond and E. R. Weeks, *Soft Matter*, 2012, Advanced print, DOI: 10.1039/c2sm26023a.
- 44 A. Caboussat and R. Glowinski, *J. Numer. Math.*, 2008, **16**, 107–117.
- 45 P. Poulin and J. Bibette, *Langmuir*, 1998, **14**, 6341–6343.
- 46 F. Leal-Calderon, V. Schmitt and J. Bibette, *Emulsion Science: Basic Principles*, Springer, 2nd edn, 2007.
- 47 H. Princen, *J. Colloid Interf. Sci.*, 1979, **71**, 55–66.
- 48 H. Princen, *J. Colloid Interf. Sci.*, 1980, **75**, 246–270.
- 49 H. Princen, *J. Colloid Interf. Sci.*, 1983, **91**, 160–175.
- 50 J. Zhou, *PhD thesis*, University of Massachusetts, Amherst, 2008.
- 51 H. A. Janssen, *Vereins Deutsch Ing*, 1895, **39**, 1045–1049.
- 52 M. D. Lacasse, G. S. Grest and D. Levine, *Phys. Rev. E*, 1996, **54**, 5436–5446.
- 53 O. Pouliquen, M. Belzons and M. Nicolas, *Phys. Rev. Lett.*, 2003, **91**, 014301.